

A POLARIMETRIC APPROACH FOR CONSTRAINING THE DYNAMIC FOREGROUND SPECTRUM  
FOR COSMOLOGICAL GLOBAL 21-CM MEASUREMENTSBANG D. NHAN<sup>1,2,5</sup>, RICHARD F. BRADLEY<sup>2,3,4</sup>, AND JACK O. BURNS<sup>1</sup>(Dated: January 19, 2017)  
Draft version January 19, 2017

## ABSTRACT

The cosmological global (sky-averaged) 21-cm signal is a powerful tool to probe the evolution of the intergalactic medium (IGM) in high-redshift Universe ( $z \leq 6$ ). One of the biggest observational challenges is to remove the foreground spectrum which is at least four orders of magnitude brighter than the cosmological 21-cm emission. Conventional global 21-cm experiments rely on the spectral smoothness of the foreground synchrotron emission to separate it from the unique 21-cm spectral structures in a single total-power spectrum. However, frequency-dependent instrumental and observational effects are known to corrupt such smoothness and complicates the foreground subtraction. We introduce a polarimetric approach to measure the projection-induced polarization of the anisotropic foreground onto a stationary dual-polarized antenna. Due to Earth rotation, when pointing the antenna at a celestial pole, the revolving foreground will modulate this polarization with a unique frequency-dependent sinusoidal signature as a function of time. In our simulations, by harmonic decomposing this dynamic polarization, our technique produces two separate spectra in parallel from the same observation: (i) a total sky power consisting both the foreground and the 21-cm background, (ii) a model-independent measurement of the foreground spectrum at a harmonic consistent to twice the sky rotation rate. In the absence of any instrumental effects, by scaling and subtracting the latter from the former, we recover the injected global 21-cm model within the assumed uncertainty. We further discuss several limiting factors and potential remedies for future implementation.

*Subject headings:* dark ages, reionization, first stars - techniques: polarimetric - methods: observational

## 1. INTRODUCTION

A theoretical framework has established three primary transition phases in the early Universe, namely the Cosmic Dark Ages (a period between recombination at redshift  $z \sim 1,100$  and the formation of the first stars  $z \gtrsim 30$ ), the Cosmic Dawn (when the first stars ignited,  $30 \gtrsim z \gtrsim 15$ ), and the Epoch of Reionization (EoR, when the first stars and galaxies reionized the neutral hydrogen HI into singly ionized hydrogen HII between  $15 \gtrsim z \gtrsim 6$ ) (Furlanetto 2006; Pritchard & Loeb 2010; Pritchard & Loeb 2012; Liu et al. 2013; Mirocha et al. 2013). While the current theoretical models of these phases are compelling, their parameter spaces are still unconstrained by any direct observations. Detailed physics on how the first stars, black holes, and galaxies form from the primordial neutral hydrogen reservoir in the intergalactic medium (IGM) is still not well understood.

The highly redshifted HI 21-cm hyperfine line (rest frequency  $\nu_0 \sim 1,420$  MHz) provides a promising observational probe to study the high- $z$  Universe where few or none of the luminous objects are available (Furlanetto et al. 2006). This hyperfine transition happens at the 1S

ground state of the hydrogen atom when the magnetic dipole moments of the proton and electron flip from parallel (triplet state) to antiparallel (singlet state). Theory suggests that the redshifted 21-cm brightness temperature fluctuations  $\delta T_{b,21cm}(z)$  measured against the cosmic microwave background (CMB) can be parametrized as (Furlanetto 2006),

$$\delta T_{b,21cm}(z) = 27(1 - x_i)(1 + \delta) \left( \frac{\Omega_{b,0} h^2}{0.023} \right) \times \left( \frac{0.15}{\Omega_{m,0} h^2} \frac{1+z}{10} \right)^{1/2} \left( \frac{T_S - T_\gamma}{T_S} \right) \text{mK}, \quad (1)$$

where  $x_i$  is the ionized fraction of HI,  $\delta$  is the fractional overdensity,  $h$  is the Hubble parameter today in unit of  $100 \text{ km s}^{-1} \text{ Mpc}^{-1}$ ,  $\Omega_{b,0}$  and  $\Omega_{m,0}$  are the fractional contributions of baryons and matter to the critical energy density,  $T_S$  is the HI's spin temperature and  $T_\gamma = T_{\gamma,0}(1+z)$  is the CMB temperature at  $z$  with present day value  $T_{\gamma,0} = 2.725 \text{ K}$ . The 21-cm transition is observed in emission when  $T_S > T_\gamma$  and absorption otherwise. As the Universe evolves, the HI content is being depleted and the thermal environment is altered. Hence, being able to measure how the redshifted 21-cm signal strength evolves over time at the low frequency regime ( $\nu \lesssim 200 \text{ MHz}$ ), we can constrain the neutral fraction and thermal history in the IGM of the early Universe.

Most of the ground-based observational efforts in the past decades are using large interferometer arrays to measure the power spectrum of spatial fluctuations of the 21-cm brightness temperature at the end of the EoR. Such experiments include the Murchison Widefield Ar-

<sup>1</sup> Center for Astrophysics and Space Astronomy (CASA), Department of Astrophysical and Planetary Sciences, University of Colorado, Boulder, CO 80309, USA

<sup>2</sup> National Radio Astronomy Observatory (NRAO), Central Development Laboratory (CDL), Charlottesville, VA 22903, USA

<sup>3</sup> Department of Astronomy, University of Virginia, Charlottesville, VA 22903, USA

<sup>4</sup> Department of Electrical and Computer Engineering, University of Virginia, Charlottesville, VA 22903, USA

<sup>5</sup> NRAO Grote Reber Doctoral Research Fellow at CDL, bang.nhan@colorado.edu

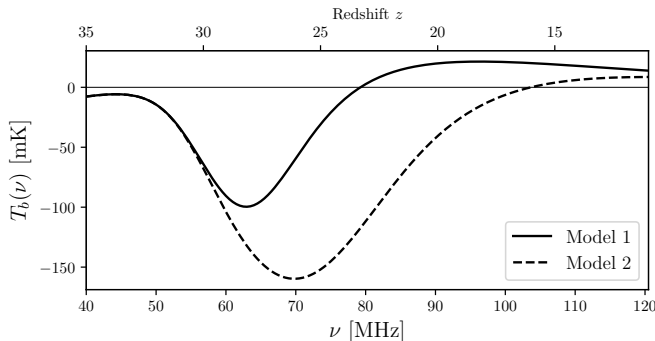


FIG. 1.— Two examples of simulated global 21-cm cosmology signal relative to the CMB. These models are generated using the Accelerated Reionization Era Simulations (ARES) code with fiducial model (solid curve, Model 1) and a factor of 10 less in the rate of X-ray heating (dashed curve, Model 2). Spectral structures of the 21-cm signal help to constrain the thermal history of the early universe between  $z$  of 35–11, which corresponds to observed frequencies of 40–120 MHz.

ray (MWA, Tingay et al. 2013; Bowman et al. 2013), the Donald C. Backer Precision Array for Probing the Epoch of Reionization (PAPER, Parsons et al. 2010), the Low Frequency Array (LOFAR, Van Haarlem et al. 2013), the Giant Metrewave Radio Telescope (GMRT, Paciga et al. 2013), the Square Kilometer Array (SKA, Mellema et al. 2013), and the Hydrogen Epoch of Reionization Array (HERA, Pober et al. 2014).

An emerging alternative approach is to utilize a single dipole antenna or a compact array consisting of a small number of antenna elements to capture the 21-cm signal evolution over a large range of frequencies ( $\sim 40 \leq \nu \leq 200$  MHz) for the aforementioned transition phases (Pritchard & Loeb 2010; Liu et al. 2013). The observed signal is spatially averaged by the broad antenna beams and is commonly known as the global (or sky-averaged) 21-cm signal. More specifically, theoretical models suggest that there are unique emission and absorption features imprinted on the global 21-cm spectrum which signify the time and physical conditions for each of the transition phases. The peak absolute amplitude of this broadband signal is predicted to range from a few tens to hundreds of millikelvin, depending on particular star formation model parameters chosen. For examples, Figure 1 illustrates how the brightness temperature  $T_b(\nu)$  varies as a function of observed frequency for two global 21-cm models, with a fiducial model (Model 1) and a factor of 10 less in the rate of X-ray heating from the universe’s first galaxies (Model 2), both generated by the Accelerated Reionization Era Simulations (ARES, Mirocha 2014). In this particular simulation, decreasing only the X-ray heating rate produces an absorption trough at higher frequency. Details on how different astrophysical parameters may alter the shape of the global 21-cm spectrum, using the similar simulation, are discussed in other studies (e.g., Mirocha et al. 2013, 2015; Mirocha et al. 2017).

At present, some of the existing ground-based global 21-cm experiments are the Experiment to Detect the Global Epoch of Reionization Signature (EDGES, Bowman & Rogers 2010), the Large-Aperture Experiment to Detect the Global the Dark Ages (LEDA, Greenhill & LEDA Collaboration 2015), the Shaped Antenna Mea-

surement of the Background Radio Spectrum (SARAS, Patra et al. 2013), the Sonda Cosmologica de las Islas para la Deteccion de Hidrogeno Neutro (SCI-HI, Voytek et al. 2014), and the Broadband Instrument for Global Hydrogen Reionization Signal (BIGHORN, Sokolowski et al. 2015a). Space-based mission concepts such as the Dark Age Radio Explorer (DARE, Burns et al. 2012) are also being proposed to carry out high precision measurements in orbit above the lunar farside for a more pristine radio environment.

Challenges arising in both observational approaches include, but not limited to, the removal of foreground emission originated from Galactic and extragalactic radio sources, ionospheric distortion, antenna beam pattern effects, instrumental systematic constraints, and terrestrial radio-frequency interference (RFI) from the weak cosmological 21-cm signal. Among these, the foreground emission is the strongest contaminant since it has an averaged brightness temperature at least four orders of magnitude stronger than the predicted 21-cm signal (Shaver et al. 1999).

At low frequencies, the foreground emission is dominated by non-thermal synchrotron radiation originated from high energy cosmic-ray (CR) electrons interacting with magnetic field in the Galaxy and other extragalactic sources (Kogut 2012). Motivated by the theory of diffusive shock acceleration (or Fermi acceleration) which predicts a power-law energy distribution for the charged particles moving in magnetized gas clouds, the observed foreground spectrum is generally parametrized as a spectrally smooth power law with a running spectral index (Shaver et al. 1999; Tegmark et al. 2000; Kogut 2012). One of a more commonly adopted parametrization is a polynomial in log-log space (Pritchard & Loeb 2010; Bowman & Rogers 2010; Harker et al. 2012) as,

$$\log \hat{T}_{fg}(\nu) = \sum_{n=0}^{m>0} c_n (\log \nu)^n \quad (2)$$

where  $\hat{T}_{fg}(\nu)$  is the estimated foreground spectrum with polynomial coefficient  $c_n$  of order  $n$ . In principle, the estimated foreground can be subtracted from the measured spectrum to reveal the global 21-cm spectrum. Instrumental systematics and other observational variations complicate the global signal extraction.

This foreground removal approach is statistically justified to extract the weak 21-cm spectrum that has distinct small-scaled frequency structure in contrast to the smoothly varying foreground (Petrovic & Oh 2011). However, this approach is limited by having to infer that the cosmological signal and foreground emission simultaneously in a single total-power spectrum. Unless the foreground spectrum is measured to a precision within few millikelvins, subtracting such a bright foreground directly from the observed-frequency space will introduce errors that are equivalent to the global 21-cm signal level (Petrovic & Oh 2011; Harker 2015). In addition, free-free emission, recombination lines, and instrumental biases can also distort the spectral smoothness of the foreground spectrum. In fact, recent studies (Bernardi et al. 2015; Mozdzen et al. 2016) find that nonlinear chromatic effects from antenna beam structures can distort the smoothness of the foreground spectrum and further

complicate the removal process.

It is desirable to have a direct means to separate and constrain the foreground spectrum from the 21-cm signal in the same observation with minimal dependence on any foreground model. Efforts in isolating the foreground from the background signal observationally have been explored in previous studies. For example, the PAPER and HERA experiments adopt the delay filtering technique in an attempt to separate the foreground in delay space instead of frequency space (Parsons et al. 2012). For the global signal, a singular value decomposition (SVD) analysis is used to construct suitable spectral basis to capture the time variable component of the measured dynamic spectra to constrain the foreground spectrum (Vedantham et al. 2013). Meanwhile, a principle component analysis (PCA) is adopted to determine contaminated spectral modes in the smooth foreground spectrum based on its spatial fluctuations (Switzer & Liu 2014).

In this study, we propose an observational technique that also utilizes the dynamic nature of the foreground to separate it from the static background through polarimetry. Projection of the anisotropic foreground source distribution induces a net polarization on a stationary dual-polarized antenna. The apparent relative motion between the Earth and the foreground modulates a unique periodic waveform to the polarization measurements that helps to constrain the foreground spectrum independently of the homogeneous background 21-cm signal. Similar modulation techniques by rotating the instrument to separate the polarization properties of instrument relative to the astrophysical sources have been shown to be effective in CMB measurements (e.g., Johnson et al. 2007; Kusaka et al. 2014). Through simulations, we demonstrate how the foreground spectrum is isolated using the projection-induced polarization and helps to extract the global 21-cm signal.

In Section 2, the general theory and rationales are presented on how the projection-induced foreground polarization can help to measure the foreground spectrum. This is followed by the mathematical formulation and an analytical example in Section 3. Simulation results using a realistic sky map are presented in Section 4. In Section 5, we discuss some of practical challenges in implementing the polarimetric approach. We conclude in Section 6 with a summary of key findings and future plans for implementing a polarimeter prototype.

## 2. GENERAL THEORY AND RATIONALES

Spatially, a majority of the diffuse foreground emission is concentrated on the Galactic plane, with extragalactic sources sparsely distributed above and below it. In the global 21-cm experiment, with the large antenna beam width, the 21-cm fluctuations with small angular scale ( $< 2^\circ$ , Bittner & Loeb 2011) are not resolvable comparing to the foreground anisotropy with larger angular scale. Hence, the observed signal is a linear combination of a relatively isotropic 21-cm background and the foreground emission.

Since conventional global 21-cm experiments have the antennas pointed toward the zenith, the foreground spectrum varies as a function of Local Sidereal Time (LST). In combination with ionospheric distortion (Vedantham et al. 2013; Datta et al. 2016; Sokolowski et al. 2015b;

Rogers et al. 2015) and RFI (Offringa et al. 2013), this temporal variations can complicate the accuracy of constraining the foreground spectrum over the course of the observation. To mitigate this, the sky measurement is averaged over a small time window, typically several sidereal hours per day to obtain a mean-valued total-power spectrum.

By recognizing the strong spatial variations in the foreground in contrast to the isotropic background, we propose a polarimetric approach that can measure the foreground spectrum without relying on any presumed sky model. For a given sky region, projection of anisotropic foreground onto the antenna plane will produce a net composite polarization. Meanwhile, the isotropic cosmological 21-cm background is not polarized due to symmetry. Noting that this projection-induced polarization is distinct from the well-known intrinsic polarization of the Galactic synchrotron emission. The Earth rotation will modulate the magnitude of the induced polarization and couple a strong periodic structure to the polarization measurement as a function time. The proposed technique is to exploit this dynamic characteristic in the induced polarization as a direct means to distinguish the foreground from the background.

Our approach consists of pointing a stationary dual-polarized antenna, a pair of crossed dipoles above a finite ground plane, at a fixed reference point in the sky about which the same sky region is observed continuously. For a ground-based experiment, this unique sky pointing can either be the North Celestial Pole (NCP) for the northern hemisphere or the South Celestial Pole (SCP) for the southern, assuming the effects of precession of the equinoxes is negligible. Without loss of generality, as the Earth rotates, the field of view (FOV) for the sky about the NCP is constant throughout the entire observation and the foreground regions appear to revolve about these two points.

The measured composite projection-induced polarization can be parametrized in terms of a net Stokes vector  $\mathbf{S}_{net}(\nu, t)$  as a function of time across the frequency range of interest, where  $\mathbf{S}_{net}(\nu, t) = \{I_{net}^\nu(t), Q_{net}^\nu(t), U_{net}^\nu(t), V_{net}^\nu(t)\}$ . The total sky intensity at each frequency, including both the background and foreground, is represented by the Stokes  $I_{net}^\nu(t)$ . The Stokes  $I_{net}^\nu(t)$  is a linearly combination of the unpolarized ( $I_u^\nu$ ) and polarized ( $I_p^\nu$ ) portion of the sky signal, hence  $I_p(t) \leq I_{net}(t)$ .

By convention, the Stokes  $\{Q_{net}^\nu(t), U_{net}^\nu(t), V_{net}^\nu(t)\}$  can be mapped in a 3-D Cartesian coordinate to form a sphere (Poincaré sphere) of radius  $R = I_p = \sqrt{Q_{net}^2 + U_{net}^2 + V_{net}^2}$ . The Stokes  $Q_{net}(t)$  measures linear polarizations at  $0^\circ$  and  $90^\circ$ , whereas the Stokes  $U_{net}(t)$  measures linear polarizations at  $\pm 45^\circ$  relative to the antenna's orientation as shown in Figure 2. The Stokes  $V_{net}(t)$  can measure any existing circular polarization with positive and negative values for left-handed and right-handed orientation, respectively.

Because the same net foreground polarization is observed twice by the same dipole after the sky revolves by  $180^\circ$  degree apart, the linear Stokes  $Q_{net}(t)$  and  $U_{net}(t)$  are sinusoidal functions with an angular frequency of twice the sky revolution rate relative to the fixed antenna. This twice-angular frequency in the Stokes

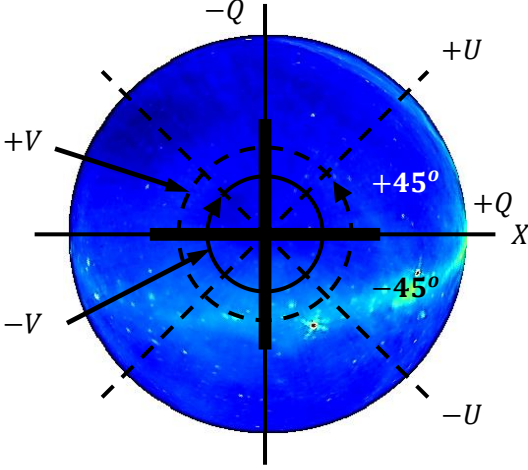


FIG. 2.— Aligning the crossed dipoles to the celestial pole, the projection-induced polarization from the foreground anisotropy can be characterized by a net composite Stokes vector in Poncaré space. The corresponding Stokes parameters  $Q$ ,  $U$ , and  $V$  measure different orientations of the polarization:  $\pm Q$  for  $0^\circ$  and  $90^\circ$ ,  $\pm U$  for  $\pm 45^\circ$ ,  $+V$  for left-handed, and  $-V$  for right-handed.

$Q_{net}(t)$  and  $U_{net}(t)$  is the dynamic feature that helps to distinguish the foreground component from the static 21-cm background. By applying harmonic analysis such as Fourier transformation to estimate the power spectral density (PSD) of these two Stokes parameters for each of the observed frequency channels, a second harmonic associated with twice the angular frequency component can be determined. The amplitude of this second harmonic can be compiled together, channel by channel, to construct a replica of the foreground spectrum. We refer this constructed spectrum as the second-harmonic Stokes spectrum hereafter.

Meanwhile, the constant total intensity  $I_{net}^\nu(t)$  contains both the background 21-cm signal and foreground emission, as in the case of the conventional total-power measurement approach, is the zero-frequency component in the PSD. In a similar manner as above, the total power Stokes spectrum can be constructed. As a result, the zeroth harmonic Stokes spectrum contains both the background and foreground signal, whereas the second-harmonic Stokes spectrum only captures information about the foreground. In principle, scaling and subtracting the second-harmonic Stokes spectrum from the total-power spectrum can recover the embedded 21-cm signal. Mathematical details and simulations are presented in the following sections.

### 3. FOREGROUND SPECTRUM CONSTRAINTS WITH PROJECTION-INDUCED POLARIZATION

#### 3.1. Stokes formalism

Consider a coordinate system fixed to the sky and a pair of crossed-dipole antennas with their boresight aligned along the  $z$ -axis at  $\theta = 0^\circ$  and the horizon is at  $\theta = 90^\circ$  on the  $xy$ -plane for the antenna's coordinate system. We further assume that the sky coordinate is not observable below the horizon at  $\theta \leq 90^\circ$ , although the ionosphere can extend the visible sky below the horizon due to refraction in the low frequencies (e.g., Vedantham et al. 2013). From a given direction  $(\theta, \phi)$  in the sky at a given instant, the broadband incoming unpolarized radio signal can be represented as quasi-

monochromatic electric field with polar and azimuthal components  $\mathbf{E}_{in}(\theta, \phi, \nu) = \{E_\theta(\theta, \phi, \nu)\hat{\theta} + E_\phi(\theta, \phi, \nu)\hat{\phi}\}$ . The incoming  $E$ -field is projected and received by the crossed dipoles, which have an  $X$  and  $Y$  oriented  $E$ -fields that are orthogonal to each other. The observed field,  $\mathbf{E}_{out}(\theta, \phi, \nu)$  in Cartesian coordinates for such a system, is a product of the incoming field with a Jones matrix (Trippe 2014),

$$\begin{aligned} \mathbf{E}_{out}(\theta, \phi, \nu) &= E_X(\theta, \phi, \nu)\hat{\mathbf{x}} + E_Y(\theta, \phi, \nu)\hat{\mathbf{y}} \\ &= [\mathbf{J}_{ant}^X(\theta, \phi, \nu) + \mathbf{J}_{ant}^Y(\theta, \phi, \nu)] \mathbf{E}_{in}(\theta, \phi, \nu) \\ &= \mathbf{J}_{ant}(\theta, \phi, \nu) \mathbf{E}_{in}(\theta, \phi, \nu) \end{aligned} \quad (3)$$

where the superscripts on the Jones matrices indicate the  $X$  and  $Y$  dipoles. In a realistic system, the Jones matrix also describes other instrumental systematics as well as external influences on the electric field such as ionospheric effects (Kraus 1986; Heiles 2002; Trippe 2014). Here, we only consider the projection of the incoming  $E$ -field onto the dipole antennas, which is described by  $\mathbf{J}_{ant}$ .

The antenna Jones matrix  $\mathbf{J}_{ant}$  is the composite far-field patterns of both crossed dipoles at each frequency, which is represented as,

$$\begin{aligned} \mathbf{J}_{ant}(\theta, \phi, \nu) &= \begin{bmatrix} J_\theta^X & J_\phi^X \\ J_\theta^Y & J_\phi^Y \end{bmatrix}_{(\theta, \phi, \nu)} \\ &= \begin{bmatrix} |E_\theta^X| e^{j\Phi_\theta^X} & |E_\phi^X| e^{j\Phi_\phi^X} \\ |E_\theta^Y| e^{j\Phi_\theta^Y} & |E_\phi^Y| e^{j\Phi_\phi^Y} \end{bmatrix}_{(\theta, \phi, \nu)} \end{aligned} \quad (4)$$

where the complex far-field components for the  $X$  and  $Y$  oriented dipoles are given in terms of their magnitude  $|E|$  and phase  $\Phi$  for each direction  $(\theta, \phi)$ .

Components of the Stokes vector at a given direction can be calculated as linear combinations of the observed  $E$ -field's autocorrelation and cross-correlation,

$$\begin{aligned} I_{out}^\nu(\theta, \phi) &= \langle E_X E_X^* \rangle + \langle E_Y E_Y^* \rangle \\ Q_{out}^\nu(\theta, \phi) &= \langle E_X E_X^* \rangle - \langle E_Y E_Y^* \rangle \\ U_{out}^\nu(\theta, \phi) &= \langle E_X E_Y^* \rangle + \langle E_X^* E_Y \rangle \\ V_{out}^\nu(\theta, \phi) &= j(\langle E_X E_Y^* \rangle - \langle E_X^* E_Y \rangle) \end{aligned} \quad (5)$$

where the bracket represents a time average of the product between the observed  $E$ -field components and their complex conjugates, with  $j = \sqrt{-1}$ . The spatial and frequency dependence on the  $E$ -field are suppressed for the ease of reading.

Assuming the  $E$ -field from all directions add incoherently, the net composite field measured at the crossed dipoles are sums of squares instead of the square of sums of individual electric field. Hence, the Stokes vector representing the projection-induced polarization of the foreground at a given instant is a vector summation of the individual Stokes vectors from each direction on the



Poincaré sphere,

$$\begin{aligned}
I_{net}^\nu &= \frac{1}{\Omega_{XY}} \sum_{\phi=0}^{2\pi} \sum_{\theta=0}^{\pi/2} I_{out}^\nu(\theta, \phi) \Delta\Omega \\
Q_{net}^\nu &= \frac{1}{\Omega_{XY}} \sum_{\phi=0}^{2\pi} \sum_{\theta=0}^{\pi/2} Q_{out}^\nu(\theta, \phi) \Delta\Omega \\
U_{net}^\nu &= \frac{1}{\Omega_{XY}} \sum_{\phi=0}^{2\pi} \sum_{\theta=0}^{\pi/2} U_{out}^\nu(\theta, \phi) \Delta\Omega \\
V_{net}^\nu &= \frac{1}{\Omega_{XY}} \sum_{\phi=0}^{2\pi} \sum_{\theta=0}^{\pi/2} V_{out}^\nu(\theta, \phi) \Delta\Omega
\end{aligned} \tag{6}$$

where  $\Omega_{XY} = \sum_{\phi=0}^{2\pi} \sum_{\theta=0}^{\pi/2} F(\theta, \phi, \nu) \Delta\Omega$  is the beam normalization factor of the averaged antenna radiation pattern  $F(\theta, \phi, \nu) = (F^X + F^Y)/2$ , where  $F^{X,Y}(\theta, \phi, \nu) = |E_\theta^{X,Y}(\theta, \phi, \nu)|^2 + |E_\phi^{X,Y}(\theta, \phi, \nu)|^2$  are the radiation patterns of antenna  $X$  and  $Y$ , with the differential solid angle element  $\Delta\Omega = \sin\theta\Delta\theta\Delta\phi$ .

### 3.2. Dynamic characteristic of the projection-induced polarization

Since the sky revolves about the celestial pole periodically every sidereal day, this dynamic characteristic is also carried over to the resulting projection-induced polarization. To illustrate this, we simplify the projection by aligning the crossed dipoles' boresight with the NCP at  $\theta = 0^\circ$ . This is analogous to placing the antenna at the Geographic North Pole (GNP, at latitude  $\phi_\oplus = 90^\circ$ ), such that the same sky revolves about the celestial pole continuously at an angular frequency  $\omega_{sky}$ , where  $\omega_{sky}/2\pi \ll \nu$ .

Because the coordinate system we adopted that is fixed to the sky, the  $(\theta, \phi)$  coincide with the declination DEC and right ascension RA in the equatorial system, respectively. As the sky revolves relative to the fixed antennas on the ground, the net induced polarization reaches its maximal or minimal values when it is parallel or orthogonal to one of the dipoles. For the same dipole, the net induced polarization is detected twice per revolution, or twice diurnal. This gives rise to the cyclic Stokes parameters  $Q_{net}^\nu(t)$  and  $U_{net}^\nu(t)$  with an angular frequency equaling twice the sky revolving rate, i.e.,  $2\omega_{sky}$ .

In such a coordinate system, the observed  $E$ -field is produced as if having the antenna rotated relative to the fixed sky. By reciprocity, we can model the antenna response coupled to the incoming  $E$ -field from direction  $(\theta, \phi)$  as one emitted by an infinitesimal horizontal crossed dipoles placed at the origin of the coordinate system. For the dipole along  $x$ -axis, the complex farfield measured at distance  $r$  has components,

$$\begin{aligned}
E_\theta^X(\theta, \phi, \nu) &\simeq -j \frac{\omega\mu I_0 l e^{-j\mathbf{k}\cdot\mathbf{r}}}{4\pi r} \cos\theta \cos\phi \\
E_\phi^X(\theta, \phi, \nu) &\simeq +j \frac{\omega\mu I_0 l e^{-j\mathbf{k}\cdot\mathbf{r}}}{4\pi r} \sin\phi
\end{aligned} \tag{7}$$

where  $\omega = 2\pi\nu$ ,  $|\mathbf{k}| = 2\pi/\lambda$  is the wave number of the observed wavelength,  $\mu$  is the permeability, and  $I_0$  is the current excited across the infinitesimal dipole with

length  $l$  by the source (Balanis 2016). Similarly, for the  $y$ -oriented dipole, components of the corresponding farfield are,

$$\begin{aligned}
E_\theta^Y(\theta, \phi, \nu) &\simeq -j \frac{\omega\mu I_0 l e^{-j\mathbf{k}\cdot\mathbf{r}}}{4\pi r} \cos\phi \\
E_\phi^Y(\theta, \phi, \nu) &\simeq -j \frac{\omega\mu I_0 l e^{-j\mathbf{k}\cdot\mathbf{r}}}{4\pi r} \cos\theta \sin\phi
\end{aligned} \tag{8}$$

As the sky revolves about the boresight of the antenna over some time  $t$ , a sky emission from direction  $(\theta_0, \phi_0)$ , that is originally coupled to the antenna response at  $(\theta_0, \phi_0)$ , is now received to the antenna response  $(\theta', \phi') = (\theta_0, \phi_0 + \omega_{sky}t)$ . By substituting the fields from Equation (8) into Equation (3) to (5), the resulting Stokes parameters corresponding to  $(\theta, \phi)$  is a function of time and are written as,

$$\begin{aligned}
I_{out}^\nu(\theta, \phi, t) &= g_0^2 (E_\theta^2 \cos^2\theta + E_\phi^2) \\
Q_{out}^\nu(\theta, \phi, t) &= g_0^2 (E_\theta^2 \cos^2\theta - E_\phi^2) \cos(2\omega_{sky}t) - \\
&\quad 2g_0^2 E_\theta E_\phi \cos\theta \sin(2\omega_{sky}t) \\
U_{out}^\nu(\theta, \phi, t) &= g_0^2 (E_\theta^2 \cos^2\theta - E_\phi^2) \sin(2\omega_{sky}t) + \\
&\quad 2g_0^2 E_\theta E_\phi \cos\theta \cos(2\omega_{sky}t) \\
V_{out}^\nu(\theta, \phi, t) &= 0
\end{aligned} \tag{9}$$

where  $g_0 = \omega\mu I_0 l / 4\pi r$ , noting that the incoming  $E$ -field components are time independent. The net induced polarization, which is estimated by the vector sum of all Stokes vectors from all direction above the horizon as Equation (6), subsequently consists of this twice-diurnal component as a function of time. This is the dynamic feature that we exploit to measure the foreground separately from the static background.

It is trivial that the net polarization can become relatively small, if not zero, when the overall foreground anisotropy decreases. For example, if the incoming  $E$ -field components are identical for all direction, the vector sum of the Stokes vectors reduces to zero. This is similar to the symmetry argument for the isotropic background signal. As a result, the magnitude of twice diurnal component can be altered. However, this is very unlikely in a real observation except for some extreme cases, such as horizon obstruction at low latitude discussed in Section 5.6. A more comprehensive analysis is elaborated through simulations with a realistic foreground map in Section 4 and discussions in Section 5.

### 3.3. Harmonic analysis and Stokes spectra

For a continuous signal  $g(t)$ , its PSD can be estimated by the Fourier decomposition in the frequency domain. For discrete signal data with length of  $N$  and sampling interval  $\Delta t$ , one of the optimized PSD estimates (Heinzel et al. 2002) is,

$$S_g^\nu(f) = \frac{(\Delta t)^2}{s_1^2} \left| \sum_{t=1}^N w(t) g(t) e^{-j2\pi f t} \right|^2 \tag{10}$$

where the window function  $w(t)$  prevents spectral leakage between frequency channels in the PSD, and the normalization factor  $s_1 = \sum_{t=0}^N w(t)$ . In this paper, we adopt the commonly used Blackman-Harris window function for the PSD calculations. At each observed frequency,

a Stokes PSD can be estimated by replacing  $g(t)$  with each of the Stokes parameters. Here we explicitly denote the dynamic frequency as  $f$  to distinguish it from the observed frequency  $\nu$ . In the context of the sky rotation,  $f = \omega_{sky}/2\pi$ .

A harmonic of order  $n$  will appear in the PSD if  $g(t)$  consists of a frequency component at  $f$ , where  $n = 1/(fN\Delta t)$ . Hence, the available power associated to the components of twice the angular frequency in Stokes  $Q_{net}(t)$  and  $U_{net}(t)$  are estimated as  $S_Q^\nu(n=2)$  and  $S_U^\nu(n=2)$ . Meanwhile, in case of the constant total intensity from  $I_{net}^\nu(t)$ , the power is located at the zeroth harmonic  $S_I^\nu(n=0)$ .

Since the  $\nu$ -dependence of the Stokes parameters is not affected by the Fourier transformation, the spectral dependence of the sky measurement is carried over to the Stokes PSD. The measured  $S_Q^\nu(n=2)$  and  $S_U^\nu(n=2)$  originated from the dynamic component of the foreground polarization are model-independent, high-fidelity, and scalable replicas of the foreground spectrum, which do not contain any contribution from the isotropic 21-cm background. The static background combined with the foreground is measured at the zero-frequency component of the total intensity spectrum  $S_I^\nu(n=0)$ .

### 3.4. Foreground subtraction with induced Stokes spectra

The sky-averaged antenna temperature  $T_{ant}(\nu)$  for a given antenna radiation pattern  $F(\theta, \phi, \nu)$  is defined as,

$$T_{ant}(\nu) = \frac{\int_0^{2\pi} \int_0^{\pi/2} T_{sky}(\nu, \theta, \phi) F(\theta, \phi, \nu) \sin \theta d\theta d\phi}{\int_0^{2\pi} \int_0^{\pi/2} F(\theta, \phi, \nu) \sin \theta d\theta d\phi} \quad (11)$$

where  $T_{sky}(\nu, \theta, \phi)$  is the brightness temperature distribution of the total sky (Kraus 1986; Wilson et al. 2009). In an ideal case, the sky temperature is simply a linear combination of the foreground emission  $T_{fg}(\nu)$  and the background 21-cm signal  $\delta T_{b,21cm}(\nu)$ . The total-power spectrum at zero-frequency  $S_I^\nu(n=0)$  is equivalent to  $T_{ant}(\nu)$  and can be parametrized as,

$$S_{I,0}^\nu \equiv S_I^\nu(n=0) = A_1 k_B [T_{fg}(\nu) + \delta T_{b,21cm}(\nu)] + A_0 \quad (12)$$

Similarly, the second-harmonic Stokes spectra are,

$$\begin{aligned} S_{Q,2}^\nu &\equiv S_Q^\nu(n=2) = B_1 k_B T_{fg}(\nu) + B_0 \\ S_{U,2}^\nu &\equiv S_U^\nu(n=2) = C_1 k_B T_{fg}(\nu) + C_0 \end{aligned} \quad (13)$$

where the  $A$ s,  $B$ s, and  $C$ s are the scaling factors and offsets. In practice, these scaling coefficients are corrupted by instrumental effects and become frequency-dependent. By assuming optimal instrument calibration, the coefficients can be treated as constants for the purpose of this paper.

Since all the Stokes spectra are measured simultaneously in the same observation, by solving for the scaling factors, the foreground spectrum can be subtracted to extract the background signal, without the need of high-order polynomial fitting using, for instance, Equation (2). Although either equation in Equation (13) can be used to solve for  $T_{fg}$  because both Stokes  $Q_{net}(t)$  and  $U_{net}(t)$  measure the same linear polarization but with a phase difference of  $90^\circ$ , using both measurements at the same time can improve the precision of the  $n=2$  har-

monic since we know both Stokes parameters share the same angular frequency component and a unique relative phase difference of  $90^\circ$  apart.

For simplicity, without loss of generality, by substituting the  $Q$ -spectrum into Equation (12) and solve for the background signal, so we have,

$$\delta T_{b,21cm}(\nu) = \frac{1}{k_B} \left( \frac{S_{I,0}^\nu - A_0}{A_1} - \frac{S_{Q,2}^\nu - B_0}{B_1} \right) \quad (14)$$

though utilizing both Stokes measurement, along with Stokes  $V$  measurement, can be useful in practice. We can obtain a relation between  $A_1$  and  $B_1$  by taking the derivative on both sides of Equation (14) as,

$$\frac{A_1}{B_1} = \left[ \frac{dS_{I,0}^\nu}{d\nu} - A_1 k_B \frac{d\delta T_{b,21cm}(\nu)}{d\nu} \right] \left( \frac{dS_{Q,2}^\nu}{d\nu} \right)^{-1} \quad (15)$$

If the global 21-cm spectrum consists of an absorption feature at  $\nu_{min}$  as predicted by the models such as ones shown in Figure 1, there exists a global minimum at  $\nu_{min}$  that can be determined by its first and second derivatives as shown in Figure 3. Hence, we can solve for  $A_1/B_1$  based entirely on the derivatives of the measured Stokes spectra since the derivative of  $\delta T_{b,21cm}(\nu)$  is zero if we evaluate Equation (15) at  $\nu_{min}$

$$\frac{A_1}{B_1} = \frac{dS_{I,0}^\nu}{d\nu} \left( \frac{dS_{Q,2}^\nu}{d\nu} \right)^{-1} \bigg|_{\nu=\nu_{min}} \quad (16)$$

In principle, the first derivatives of the emission features at the higher end of the passband in Figure 1 also provide a zero crossing to constrain  $A_1/B_1$ . However, the emission feature is more likely to be outside the band since it is predicted to be broader and less prominent than the absorption one.

By comparing (15) and (16), it is apparent that the sources of error in solving for  $A_1/B_1$  are the accuracy in estimating the derivatives of the measured Stokes spectra as well as determining  $\nu_{min}$ . In general, there exists truncation error in numerical differentiation in the order of the frequency step size  $\mathcal{O}(\Delta\nu)$  (Hamming 2012). Hence, keeping the spectral resolution low can improve the accuracy of calculating the derivatives. However, determining the frequency of the absorption feature in the global 21-cm signal is not straightforward since the background signal is unknown. Possible ways helping to constrain  $\nu_{min}$  and the sensitivity of this scheme are further discussed in Section 5.2 and Section 5.3. It is worth noting that the foreground removal discussed here only applies when the an absorption feature exists in the observing band as predicted by theory ( $\sim 40 < \nu < 200$  MHz).

## 4. SIMULATIONS WITH A REALISTIC FOREGROUND MAP

### 4.1. Simulation description

In this section, we illustrate how the projection-induced polarization from a realistic sky map can give rise to the second-harmonic spectrum and how a model global 21-cm spectrum can be recovered using the procedure presented in the previous section.

For simplicity, the broad farfield beam patterns of the crossed dipoles are approximated by circular Gaussian beams. Referencing from the typical antenna beam

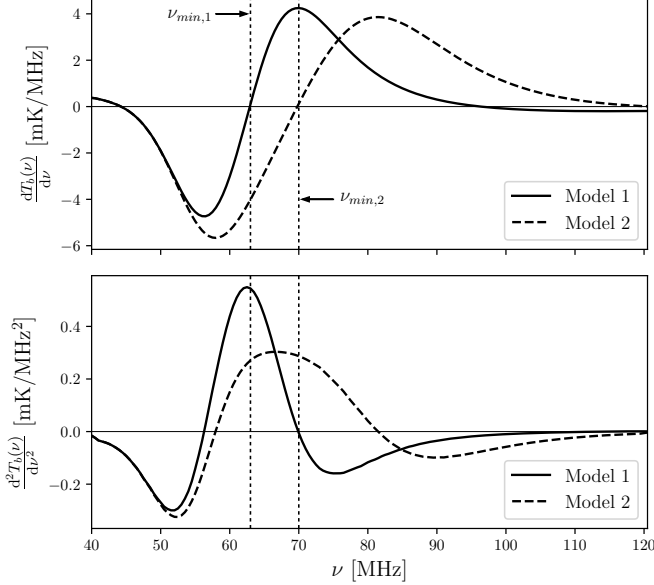


FIG. 3.— *Upper*: Zero crossings of the first derivatives of the ARES global 21-cm Model 1 (solid curve) and 2 (dashed curve) from Figure 1 help to determine their global minima at  $\nu_{min,1}$  and  $\nu_{min,2}$  (vertical dashed lines) respectively. These global minima help to obtain the coefficients to scale the second-harmonic spectrum  $S_{Q,2}^\nu$  up to the total power spectrum  $S_{I,0}^\nu$  for foreground subtraction. *Lower*: Magnitudes of the second derivatives of the models help to differentiate potential local minima from the global minima required for the scaling coefficients.

sizes from other global 21-cm experiments like EDGES (Mozdzen et al. 2016), we adopt a full width at half maximum (FWHM) of  $60^\circ$  for the Gaussian beams.

The Gaussian beams are centered at the NCP of a set of foreground maps which are extrapolated from the Haslam full-sky survey at 408 MHz, as shown in Figure 4 (Haslam et al. 1982), to 40-120 MHz using a power-law parametrization with a mean spectral index  $\beta = 2.47$  as suggested by previous observations (Bowman et al. 2008),

$$T_{fg}(\theta, \phi, \nu) = T_{\text{Haslam}}(\theta, \phi) \left( \frac{\nu}{408 \text{ MHz}} \right)^{-\beta} \quad (17)$$

For each of the ARES global 21-cm model, at each frequency, an isotropic 21-cm background map of brightness temperature  $\delta T_{b,21cm}(\nu)$  for all directions is linearly combined with the foreground map  $T_{fg}(\nu, \theta, \phi)$ . Since the spatial resolution is not critical in the global 21-cm measurement, it is sufficient to set the spatial resolution of both the beam patterns and the sky map to  $1^\circ \times 1^\circ$  in our simulations. We also assume the Gaussian beams to be frequency independent across the passband, which is not necessarily true for the real antenna beams.

Although intrinsic linear polarization is known to exist in the Galactic synchrotron foreground, we assume the foreground itself to be unpolarized (or randomly polarized) in the simulations since the sky-averaged intrinsic polarization is expected to be less dominant than net projection-induced polarization. For completeness, both the chromatic beam effects and intrinsic polarization are elaborated in Section 5.

For an unpolarized foreground, half of the averaged total power is equally received by each of the antenna

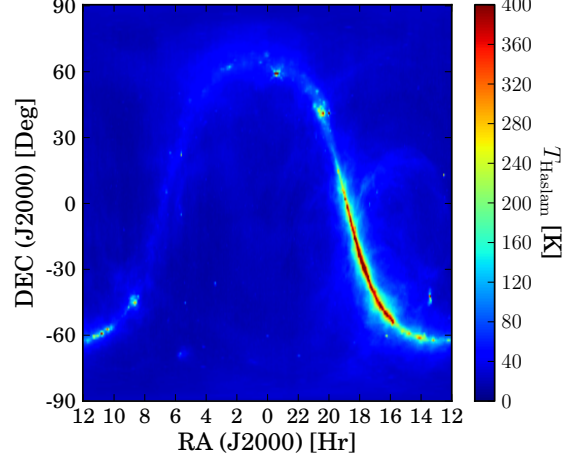


FIG. 4.— The realistic foreground between 40-120 MHz is extrapolated from the Haslam full-sky map at 408 MHz, as shown here, with a spectral index  $\beta$  of 2.47.

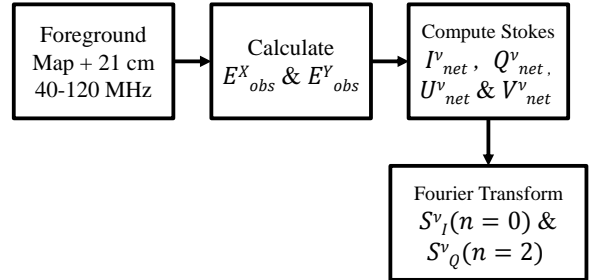


FIG. 5.— Summary for the simulations and analysis procedures that allows the foreground spectrum be separated from the isotropic 21-cm background by exploiting the dynamic characteristic in the projection-induced foreground polarization.

polarization. According to the formalism presented in Section 3.1, we estimate the incoming  $E$ -field from the foreground as  $\mathbf{E}_{in}(\theta, \phi, \nu) = \{E_0(\theta, \phi, \nu)\hat{\theta} + E_0(\theta, \phi, \nu)\hat{\phi}\}$  where  $E_0(\theta, \phi, \nu) = \sqrt{k_B T_{fg}(\theta, \phi, \nu)/2}$  with the Boltzmann constant  $k_B$ .

#### 4.2. Simulation results

After the observed  $E$ -field is calculated as in Equation (3), the net Stokes parameters are computed as the foreground revolves about the NCP at a rate of one cycle per 24 sidereal hours. The resulting Stokes parameters are Fourier transformed to compute the PSD. Zeroth- and second-harmonic spectra,  $S_{I,0}^\nu$  and  $S_{Q,2}^\nu$ , are constructed by assembling the magnitude of the FFT output at  $n = 0$  and  $n = 2$  for all frequencies. Figure 5 summarizes the basic steps to produce the Stokes spectra.

For a circular beam, the same sky region is observed continuously over time as the foreground revolves about the NCP, hence the  $I_{net}^\nu(t)$  is constant at each frequency as shown in Figure 6. This translates to a zero-frequency component in its periodogram as shown in Figure 7. In contrary, the linear net polarization represented by the Stokes  $Q_{net}^\nu(t)$  is a sinusoidal function with angular frequency that equals twice the sky's revolution rate, or two cycles per 24 sidereal hours, as illustrated in Fig-

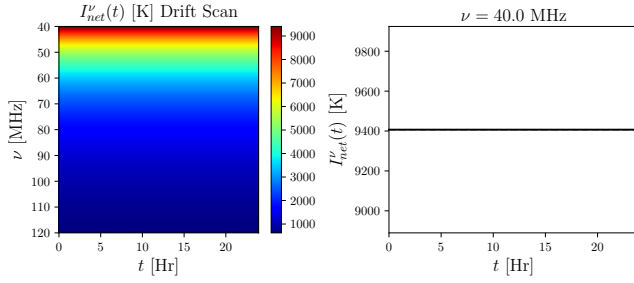


FIG. 6.— *Left*: Stokes  $I_{net}$  drift scan for Haslam foreground example with circular Gaussian beams with the time on the  $x$ -axis and the observed frequencies on the  $y$ -axis. *Right*: An example of the Stokes  $I_{net}$  which is constant for all time at  $\nu = 40$  MHz. This total intensity measurement contains both the foreground and background signal.

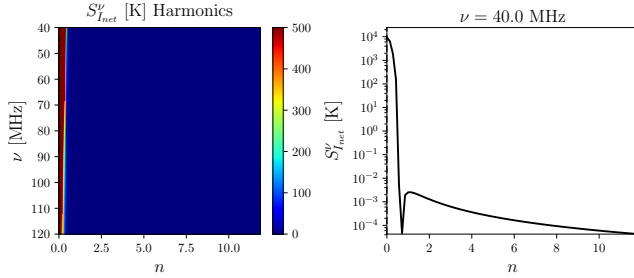


FIG. 7.— *Left*: The FFT of the Stokes  $I_{net}$  are shown in terms of harmonic order  $n$  as a function of observed frequencies. *Right*: The total available power for the constant Stokes  $I_{net}$  can be found at harmonic  $n = 0$ . The zeroth-harmonic Stokes spectrum  $S^{\nu}_{I,0}$  is constructed by assembling the magnitude at  $n = 0$  across the 40-120 MHz band.

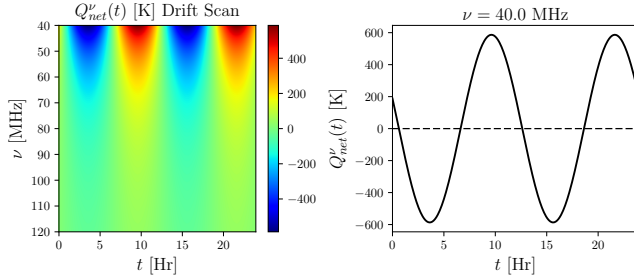


FIG. 8.— *Left*: Stokes  $Q_{net}$  drift scan for Haslam foreground example with circular Gaussian beams with the time on the  $x$ -axis and the observed frequencies on the  $y$ -axis. *Right*: The projection-induced polarization is modulated by a sinusoidal waveform with angular frequency of twice the sky rotation rate at each observed frequency, as shown here for  $\nu = 40$  MHz. This dynamic characteristic is unique to the foreground and can be used to separate it from the static background so the spectral structures of the foreground spectrum can be constrained without assuming any sky model.

ure 8. Subsequently, its periodogram consists of only a harmonic at  $n = 2$  in Figure 9. This second harmonic only arises from the anisotropy in the foreground map. Hence by constructing a second-harmonic spectrum  $S^{\nu}_{Q,2}$  in a manner similar to  $S^{\nu}_{I,0}$ , we obtain a replica of the foreground spectrum, free from any isotropic background signal. This is confirmed by calculating the spectral index  $\beta$  recovered from the  $S^{\nu}_{Q,2}$ , which is found to be identical to the input  $\beta$  of 2.47 in Figure 10.

In this ideal scenario, where instrumental systematics and other contaminations can be removed, the total power spectrum is identical to  $S^{\nu}_{I,0}$  so  $A_1$  is unity with zero offset  $A_0$ . Since  $S^{\nu}_{Q,2}$  is a scalable replica of the the

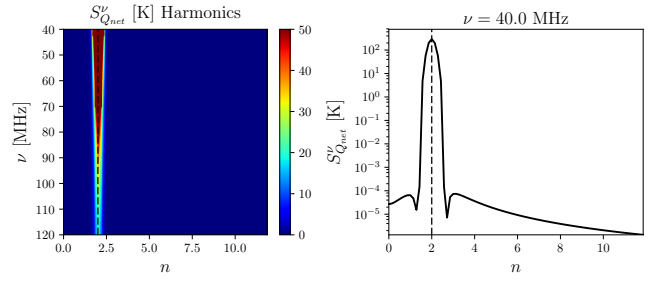


FIG. 9.— *Left*: Similar to the total intensity measurement, FFT of the Stokes  $Q_{net}$  helps to distinguish different harmonic components function of observed frequencies. *Right*: The second-harmonic Stokes spectrum  $S^{\nu}_{Q,2}$  can be constructed by assembling the magnitude at  $n = 2$  across the band of interest. This resulting spectrum contains only the foreground but not the background 21-cm signal.

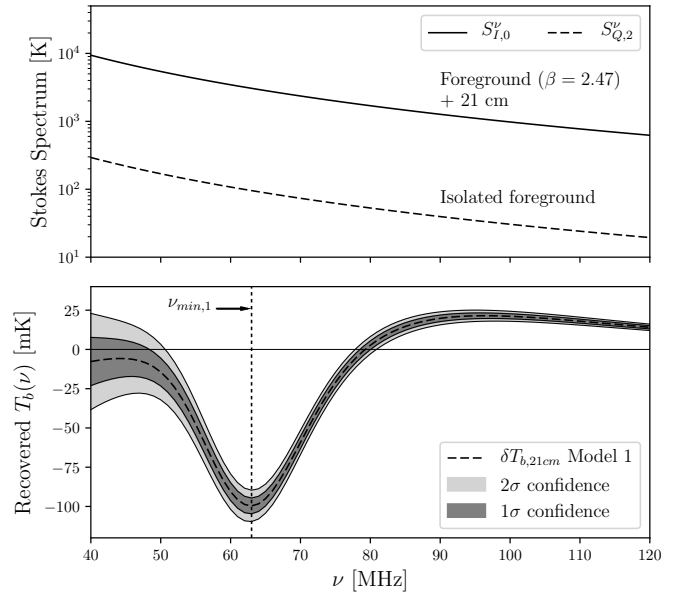


FIG. 10.— *Upper*: The Stokes spectrum  $S^{\nu}_{Q,2}$  (dashed curve) is shown to have a spectral index identical to the input value  $\beta$  of 2.47. By scaling and subtracting this spectrum from the total intensity spectrum  $S^{\nu}_{I,0}$  (solid curve), the background 21-cm signal can be retrieved. *Lower*:  $1\sigma$  and  $2\sigma$  confidence levels of the extracted 21-cm spectrum is compared to the input ARES spectrum for Model 1 (dashed curve). The primary uncertainty in this result is due to error in estimating  $\nu_{min,1}$  (vertical dashed line) for the first derivative of Model 1 to compute the scaling factor  $1/B_1$  of Equation (16).

foreground spectrum, only the scaling coefficient  $B_1$  is needed and no offset value  $B_0$  is expected. After scaling the  $S^{\nu}_{Q,2}$  up to the  $S^{\nu}_{I,0}$  with  $B_1$  as in Equation (16), the foreground spectrum is subtracted to reveal the underlying global 21-cm model with Equation (14), as shown in Figure 10 and Figure 11.

In this simulation, we assume that the Stokes measurements have been integrated long enough to achieve a minimal measurement precision and the only remaining error in the extracted 21-cm model is the uncertainty  $\sigma_{AB}$  from determining the scaling factor  $A_1/B_1$ , or  $1/B_1$  in this case. Details on error propagation is elaborated in following section.

## 5. IMPLEMENTATION ASPECTS

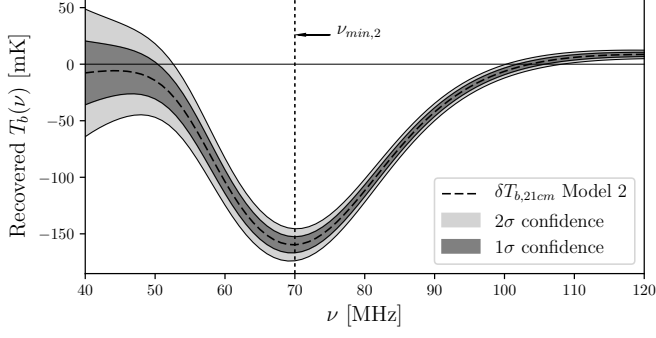


FIG. 11.—  $1\sigma$  and  $2\sigma$  confidence levels of the extracted 21-cm spectrum is compared to the input ARES spectrum for Model 2 (dashed curve). The primary uncertainty in this result is due to error in estimating  $\nu_{min,2}$  (vertical dashed line) for the first derivative of Model 2 to compute the scaling factor  $1/B_1$  of Equation (16).

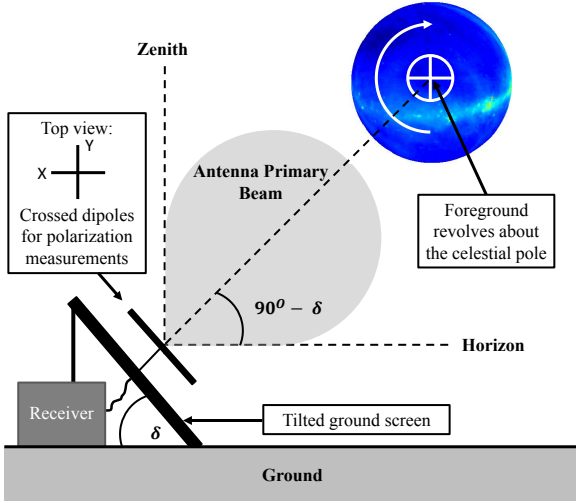


FIG. 12.— Schematic for the ground-based polarimeter, which consists of a pair of tilted crossed dipoles pointing at a celestial pole. The primary differences between this polarimetric approach and other global 21-cm experiments are full-Stokes measurements and its configuration to separate the foreground from the static background through its own dynamic characteristic. The tilt angle  $\delta$  corresponds to the observer's latitude.

We have demonstrated that, with idealized circular Gaussian beams, the second-harmonic spectra originated from the dynamic component of the projection-induced polarization can be used to track the foreground spectrum, isolated from the static 21-cm background. In this section, we assess some of challenges when implementing such polarimetric approach in practice. A general layout of implementing such instrument on the ground consists of a pair of crossed dipoles being tilted such that its bore-sight is pointing toward a celestial poles as illustrated in Figure 12.

### 5.1. Foreground subtraction error propagation

As mentioned in Section 3.4, the dominant sources of error originate from estimating the derivatives of the Stokes spectra as well as determining the  $\nu_{min}$  at which the first derivative of absorption feature in the background signal vanishes. Because both errors are functions of the frequency resolution, the confidence levels on the

extracted Model 1 and Model 2 as shown above are attributed to the resolution chosen for this simulation, i.e.,  $\Delta\nu = 1$  MHz.

Assuming the absorption feature exists at  $\nu_{min}$  within the instrument's passband, but the estimated  $\nu'_{min} = \nu_{min} \pm \Delta\nu$  with error  $\Delta\nu$  is used for Equation (15), then a non-zero  $d\delta T_{b,21cm}/d\nu$  is unknowingly assumed to be zero when computing  $A_1/B_1$  with Equation (16). In fact, when evaluating Equation (15) at  $\nu'_{min} \neq \nu_{min}$ , we obtain a non-zero value on the right-hand side (RHS) in the following equation,

$$\frac{A_1}{B_1} - \frac{dS_{I,0}^\nu}{d\nu} \left( \frac{dS_{Q,2}^\nu}{d\nu} \right)^{-1} = A_1 k_B \frac{d\delta T_{b,21cm}(\nu)}{d\nu} \left( \frac{dS_{Q,2}^\nu}{d\nu} \right)^{-1} \quad (18)$$

Since the frequency resolution of the simulations is set to 1 MHz, the first derivative of  $\delta T_{b,21cm}$  does not equal to zero exactly at the estimated  $\nu'_{min}$ . So we estimate the  $\sigma_{AB}$  to be the unknown difference between the values of  $A_1/B_1$  at the correct  $\nu_{min,1}$  and at the  $\nu'_{min}$ . This error is essentially the term on the RHS but we are not using the derivative of our input Model 1 directly.

By applying a basic error propagation to Equation (14), the uncertainty of the extracted 21-cm signal  $\sigma_{21cm}$  can be estimated as,

$$\sigma_{21cm}(\nu) = \frac{1}{k_B A_1} \left[ \sigma_{I,0}^2(\nu) + \left( \frac{A_1}{B_1} \right)^2 \sigma_{Q,2}^2(\nu) + (S_{Q,2}^\nu - B_0)^2 \sigma_{AB}^2 \right]^{1/2} \quad (19)$$

where  $\sigma_{I,0}$  and  $\sigma_{Q,2}$  are the measurement uncertainties of the Stokes spectra  $S_{I,0}^\nu$  and  $S_{Q,2}^\nu$  defined by the radiometer equation in Equation (21). In the simulations above, we assume the measurement uncertainty of the Stokes spectra have been reduced to a minimal level after longterm integration, so the overall uncertainty of the extracted signal which defines the confidence levels reduces to,

$$\sigma_{21cm}(\nu) = (S_{Q,2}^\nu - B_0) \sigma_{AB} = S_{Q,2}^\nu \sigma_{AB} \quad (20)$$

### 5.2. Searching for $\nu_{min}$

Except for the derivatives of the Stokes spectra on the left-hand side (LHS) of Equation (18), the scaling factor and the background signal's first derivative are unknowns. As an observer, we are simply searching for a frequency of the absorption feature in the background so that the second terms on the RHS vanishes even without knowing where it is. We here propose a blind search to determine an optimal  $\nu_{min}$  during the foreground subtraction. After an initial foreground subtraction by choosing a random frequency as  $\nu_{min}$  in the passband, the process of scaling and subtracting  $S_{Q,2}^\nu$  from  $S_{I,0}^\nu$  can be refined iteratively (ideally from one end of the passband to the other) until potential spectral structures may appear in the residual spectrum, as illustrated in Figure 13.

Without the background signal and its absorption feature as a priori information, the iterative scaling process only converges when it locates a zero crossing in the global 21-cm spectrum's derivative. By assuming that each of the chosen  $\nu_{min}$  can potentially be the desired

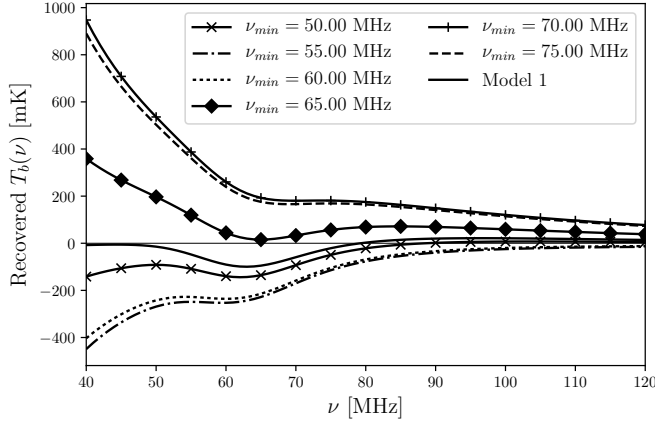


FIG. 13.— Illustration on how the scaling factor  $A_1/B_1$  can be refined iteratively by a blind search for frequency  $\nu_{min}$  of the global 21-cm absorption feature, at which its first derivative equals to zero. Shown here is a series of recovered candidates for the input 21-cm model spectrum. Each of the curve is estimated by scaling and subtracting the second-harmonic spectrum from the total-power spectrum using a  $A_1/B_1$  factor computed at an assumed  $\nu_{min}$  as shown in the legend, without using any information from the input Model 1.

value, we can simply calculate  $A_1/B_1$  by ignoring the extra term on the RHS of Equation (18). Figure 14 shows how  $A_1/B_1$  varies as a function of  $\nu_{min}$ . By the formulation of Equation (18), it is not surprising that the curve is proportional to the negative value of Model 1's first derivative in Figure 3. More importantly, since local and global minima can be distinguished by the magnitude of the second derivative, we can determine the desired  $\nu_{min,1}$  simply by taking the first derivative of  $A_1/B_1$  respect to  $\nu_{min}$ , as shown in Figure 14, without any knowledge of the background signal.

It is worth noting that the approach presented here only applies to an idealized instrument with optimized calibration, which is free from any spurious contamination and unwanted distortion. Presence of realistic instrumental systematics and other measurement uncertainties can complicate this foreground subtraction procedure. More sophisticated estimation algorithms, which utilize theoretical constraints from the 21-cm physics and instrument models in terms of the Bayesian statistics such as the Monte Carlo Markov Chain (MCMC, Harker et al. 2012; Mirocha et al. 2015) and SVD, are needed in parallel. This will be investigated in future work.

### 5.3. Stokes spectra measurement sensitivity

In the full sky simulations above, the Stokes spectra are assumed to have been integrated long enough to achieve an optimal measurement precision such that only  $\sigma_{AB}$  dominates the overall error in extracting the 21-cm models as shown in Figure 10 and Figure 11. By considering only the contribution of thermal noise after other systematics have been corrected and treating  $\sigma_{AB}$  as a second-order effect, we estimate the required integration time to achieve a  $\sigma_{I,0}/k_B$  of at least 10 part per million (ppm) of the expected sky noise temperature with the radiometer equation.

The generic radiometer equation in Equation (21) suggests the measuring uncertainty (or minimal detectable temperature change) at each frequency channel  $\Delta T_{min}(\nu)$  is dictated by the systematic noise tempera-

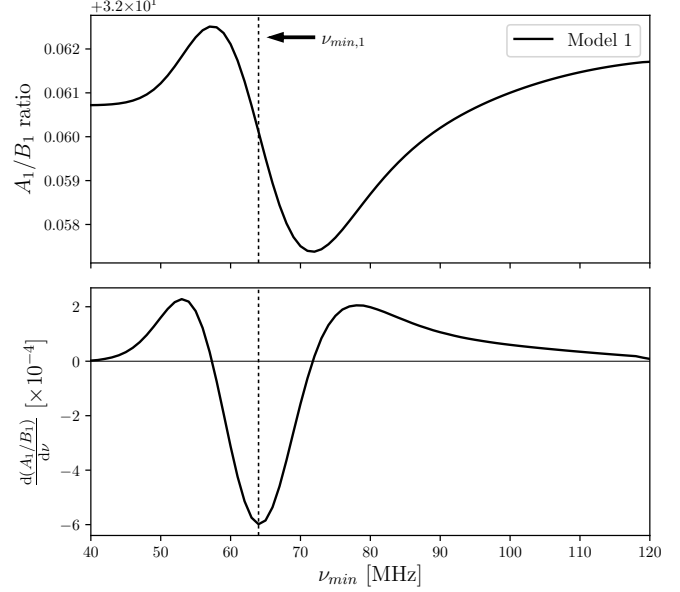


FIG. 14.— *Upper*: This illustrates how the factor  $A_1/B_1$  varies as a function of the chosen  $\nu_{min}$  during the blind search procedure. Since each chosen  $\nu_{min}$  is used by assuming it is the frequency of the absorption feature,  $A_1/B_1$  represents the unknown error contributed by the term on the RHS of Equation (18). Hence it is proportional to the negative value of the global 21-cm spectrum's first derivative. *Lower*: Since the magnitude of a second derivative helps to distinguish a local minimum from a global one, taking the first derivative of  $A_1/B_1$  respect to  $\nu_{min}$  provides an additional information to allow the iterative process to converge onto the desired  $\nu_{min,1}$  (as shown in the dashed line).

ture  $T_{sys}(\nu)$  and decreases as a function of the overall integration time  $\tau_{int}$  and the available bandwidth  $\Delta\nu$  in the absence of any receiver gain variations.

$$\Delta T_{min}(\nu) = \frac{T_{sys}(\nu)}{\sqrt{\tau_{int}\Delta\nu}} \quad (21)$$

From the simulation, at 40 MHz, the total sky temperature is about 9400 K. By assuming a receiver noise temperature  $T_{rx} = 300$  K, the total system noise temperature  $T_{sys} \sim 9700$  K. For different bandwidth value, using the radiometer equation, a rudimentary estimates of integration time as calculated. As shown in Table 1, a

TABLE 1  
INTEGRATION TIME ESTIMATES FOR DIFFERENT SPECTRAL RESOLUTION

$\Delta\nu$ [Hz]	$\tau_{int}$ [Hr]
$1.0 \times 10^4$	$2.46 \times 10^4$
$5.0 \times 10^4$	$4.92 \times 10^3$
$1.0 \times 10^5$	$2.46 \times 10^3$
$5.0 \times 10^5$	$4.92 \times 10^2$
$1.0 \times 10^6$	$2.46 \times 10^2$

reasonably short integration time is needed for  $\Delta\nu > 100$  kHz to achieve the required sensitivity under the given assumptions.

### 5.4. Chromatic beam effects

In global 21-cm experiments, it is desirable to have a broadband antenna with relatively low variations in



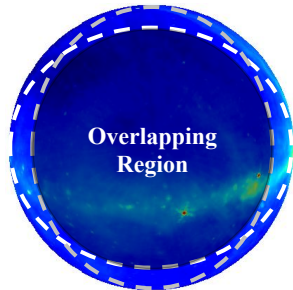


FIG. 15.— Illustration of the overlapping sky region covered by two elongated beams from the crossed dipoles. The overlapping sky region can be observed continuously by both antenna, but not the exterior regions.

the beam patterns as a function of frequency. Since the intrinsic physical size and surrounding environment of a resonant antenna structure determine the available bandwidth and its efficiency, it is unavoidable to have an antenna radiation pattern  $F(\theta, \phi, \nu)$  varies as a function of frequencies. The beam patterns are related to the antenna directive gain which determines the antenna's effective FOV. Hence, the effective collecting area is altered by the frequency dependent antenna gain, which perturbs the total observable power. This chromatic dependence of the antenna beams corrupts the spectrally-smooth foreground by introducing unwanted spectral structures into the sky measurements (Vedantham et al. 2013; Bernardi et al. 2015; Mozdzen et al. 2016).

The projection-induced polarization relies on the overall foreground anisotropy to produce a net Stokes vector, but the level of anisotropy depends on the beams' effective FOV. Hence the variations in the antenna gain with frequency will perturb the measured net Stokes vector. The spectral shape of the constructed Stokes spectra, like  $S_{I,0}'$  and  $S_{Q,2}'$ , are also therefore distorted. Depending on the magnitude of these gain variations, the resulting unwanted spectral structures can be as large as, if not greater than, the predicted global 21-cm signal.

In addition to the perturbed FOV due to the antenna gain variations, geometry of the beam patterns can also affect the spectral shape of the Stokes spectra. In practice, it is difficult to design an antenna with a circular beam across the entire passband. Due to the intrinsic characteristics of a dipole resonator, a certain level of beam elongation (or ellipticity) is often present in the beam patterns.

If the crossed dipoles have circular beams, they cover the same sky region the entire time so that the cross-correlation between the  $X$  and  $Y$  oriented antenna are identical. However, as illustrated in Figure 15, when the dipoles have two orthogonal elongated beams, only the overlapping region of the two beams covers the same sky at the entire time. This overlapping region is maximized when the two beams aligned in the case of circular ones. The sky portion outside of this overlapping region is only sampled whenever it is aligned with the dipoles. This contributes fourth-order harmonic component ( $n = 4$ ) into the Stokes parameters  $I$  and  $I_p$ . As the beam elongates differently from frequency to frequency, this introduces spectral variations to the Stokes measurements, thus to the foreground spectrum.

These chromatic distortions can compromise the de-

tection sensitivity unless the antenna beams are perfectly known. One of the probable ways to mitigate this effect is to reference the measurements to numerical antenna beam models. Careful incorporation of the antenna structure design and environment allows sophisticated electromagnetic simulation software, such as the Computer Simulation Technology (CST) or the High Frequency Structural Simulator (HFSS), to produce high-fidelity antenna beam models. By bootstrapping these beam models to the measurements, the spectral-dependent beam distortions can be mitigated, if not removed. Rudimentary analysis suggests that as long as the antenna beam pattern can be constrained with accuracy down to few tens ppm, the chromatic effects on the sky measurements can potentially be corrected to a desired level. In principle, the fourth-order harmonic is tracking the beam elongation and potentially can be used as feedback information to the beam modeling and calibration. However, the full potential of such beam correction using numerical beam model will be explored in future work.

### 5.5. Ground effects on the antenna beams

Our simulations assume a pair of crossed-dipole antennas located at the GNP (at latitude  $\phi_{\oplus} = 90^\circ$ ) to have a full FOV the northern sky centered at the NCP. For practical and logistical reasons, such an instrument can only be deployed at locations of latitude between  $0^\circ < \phi_{\oplus} < 90^\circ$ , where the Equator is at  $\phi_{\oplus} = 0^\circ$ . The antenna will be pointing toward the NCP at a tilt angle  $\delta$  which is a function of the observer's latitude.

From simple image theory formulation, it is shown that the farfield antenna beams for a horizontal dipole above a finite ground plane at height  $h$  are smooth pattern resembling the Gaussian beams (Balanis 2016). However, as the antenna and its ground plane are being tilted to point at the celestial pole, instead of a single image, multiple images of the dipole are reflected across the ground screen as well as the actual ground as illustrated in Figure 16. The different images from different propagation distances result in phase delays such that interferometric fringes are introduced into the beams. These ground effects can be mitigated by situating the antenna system on a slope instead of on the flat ground as in Figure 17. The slope angle needs to be consistent with the tilt angle  $\delta$ . Given the proposed configuration, any potential ground effects on the antenna beam will be present in the measured Stokes parameters as constant with time. It is worth noting that such beam distortion due to the ground can very likely impose a  $n = 1$  harmonic, if not at higher orders ( $n > 4$ ), to the Stokes measurement instead of at  $n = 2$  due to the relative geometry of the antenna and the sky.

### 5.6. Horizon obstruction

As the latitude decreases toward the Equator, the FOV is partially obstructed by the horizon thus the visible sky can be separated into two parts. Only the inner region of the sky about the boresight, as shown within the dashed circle in Figure 18, is observable the entire time, whereas the sky region outside the dashed circle rises and sets once per revolution.

As pointed out in previous sections, the magnitude of the second harmonic in projection-induced polarization



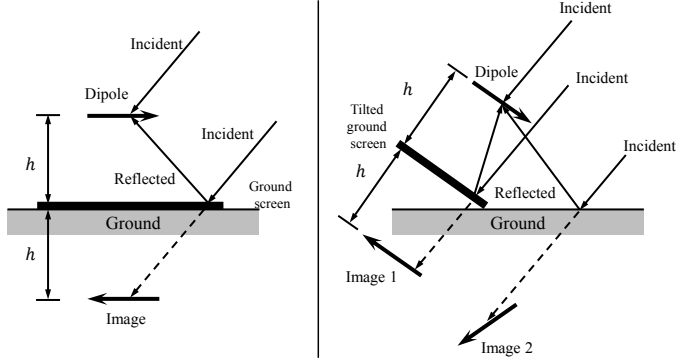


FIG. 16.— *Left*: There is a single image when the horizontal dipole is above the ground plane at a height of  $h$ . *Right*: Multiple images are present when the dipole are tilted relative to the flat ground. This introduces unwanted interferometric fringes that distort the smooth dipole beams.

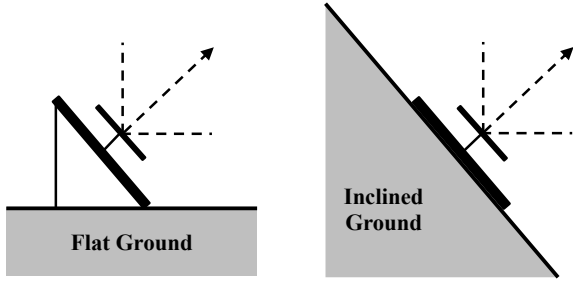


FIG. 17.— To mitigate the ground effects on the beams, the tilted dipole can be situated on an inclined ground (*Right*) with a slope similar to the tilt angle  $\delta$  instead of a flat ground (*Left*), depends on the observer's latitude.

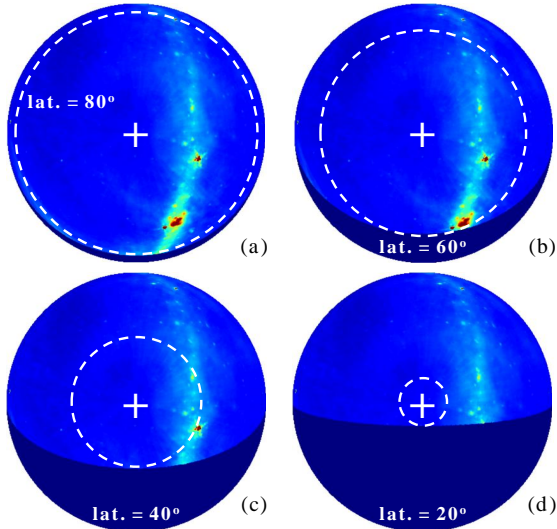


FIG. 18.— The observable sky centered at the NCP is partially obstructed by the horizon as the latitude of the observation site decreases: (a)  $\phi_{\oplus} = 80^\circ$ , (b)  $\phi_{\oplus} = 60^\circ$ , (c)  $\phi_{\oplus} = 40^\circ$ , and (d)  $\phi_{\oplus} = 20^\circ$ . As a result, the inner sky region is observable the entire time (inside the white dashed circle), whereas the outer region rises and sets once per revolution. As the inner sky region shrinks, so do the amplitude hence the SNR of the second-harmonic spectrum. A first-order harmonic is introduced to the linear Stokes parameters due to the rising and setting of the outer sky region.

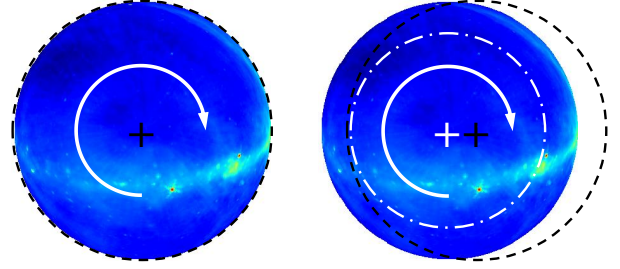


FIG. 19.— *Left*: The antenna pointing is aligned to the NCP hence the sky revolution is concentric to the antenna's field of view. *Right*: Misalignment between the antenna's boresight (black cross) and the NCP (white cross) results in only a portion of the visible sky (within the white dot-dashed circle) that is observable continuously the entire time. The white arrow indicates the orientation of the sky rotation relative to the observer.

depends on the overall anisotropy of the sky region which can be observed the entire time continuously. Hence, with the presence of the horizon, the sky region that contributes to the second harmonic in  $S_{Q,2}^{\nu}$  and  $S_{U,2}^{\nu}$  is this inner sky region within the dashed circle. As a result, smaller radii of the inner sky region at lower latitudes imply lower accuracy of the second harmonics relative to overall system noise. Additionally, as the outer sky region rises and sets, it contributes additional terms to the projection-induced polarization with angular frequency of at least once per revolution to produce a  $n = 1$  harmonic. Meanwhile, the sharp cutoff of the horizon will also introduce high-frequency components to the periodic waveforms in the Stokes parameters which can be identified at  $n > 4$  in the PSD. Similar to other effects mentioned above, although these additional harmonics can take over the power from the second harmonic and lower its sensitivity, their effects are attenuated because the antenna gain decreases at larger angles away from the boresight for the outer sky region.

By incorporating the observer's latitude, effects of the horizon obstruction on the Stokes measurement can be characterized and corrected if needed. A balance is also needed between site selection, RFI prevention, SNR of the projection-induced Stokes parameters, as well as minimal ionospheric disturbance. For example, selecting a radio-quiet zone with a latitude range that can accommodate a minimal horizon obstruction yet not close to the Earth's magnetic poles, at which strong interaction between the ionosphere and cosmic rays is well known (Newell et al. 2001). An alternative to avoid the Earth's horizon effect is to adapt this technique into a space-based instrument, such as what is being proposed for DARE.

### 5.7. Beam pointing error

By design, the accuracy of measuring the second harmonic component in the projection-induced polarization relies on the antenna pointing. If the antenna boresight is not aligned with the celestial poles, the foreground region centered at the celestial pole is not concentric with the antenna beams, as illustrated in Figure 19. As the sky revolves around, the foreground appears to “wobble” about the off-centered pointing.

Similar to the horizon obstruction, the effective sky region that produces the  $n = 2$  component (within the dot-dashed circle) is reduced which decreases the power

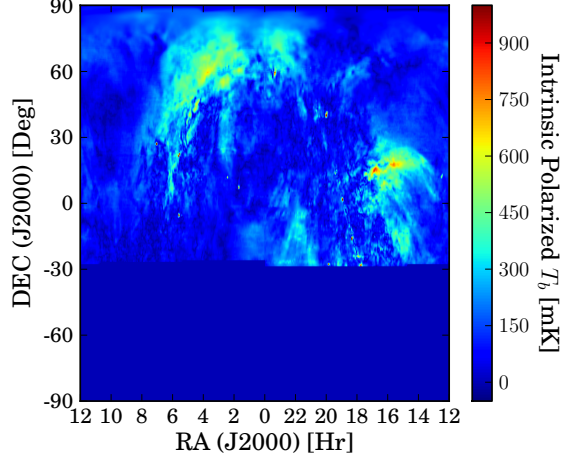


FIG. 20.— Intrinsic foreground polarized temperature map obtained from the DRAO sky survey at 1.4 GHz.

of the second harmonic spectrum thus limits the accuracy of the Stokes measurements. As the off-centered sky revolves around, amplitudes and angular frequencies of the Stokes parameters are modulated such that additional harmonics are introduced in their PDS, for example an additional  $n = 4$  component can be introduced to the measured intensity  $I$  and  $I_p$ . These modulations depend on the frequency-dependent beam sizes, hence they will also cause unwanted spectral structures to appear in the measured sky spectrum because the modulations correlate to the frequency-dependent beam sizes. Being said, these effects can easily be mitigated by improving the pointing accuracy. Based on our simulations, we find that the error is acceptable for a pointing error of  $1^\circ$  or less relative to the celestial pole based.

### 5.8. Effects of intrinsic foreground polarization

Synchrotron emission Galactic foreground is well known to have a linearly polarized component. As an example, Figure 20 illustrates the spatial distribution of the intrinsic foreground polarized brightness temperature observed from the DRAO 1.4 GHz sky survey (Wolleben et al. 2006).

As the polarized incoming signal propagates through the magnetized interstellar medium (ISM), the polarization angle of the signal rotates, which is known as Faraday rotation. In Gaussian cgs units, the change in propagation phase angle is given as (Wilson et al. 2009),

$$\Delta\psi = \lambda^2 \text{RM} = \frac{e^2}{2\pi m_e^2 c^2} \frac{1}{\nu^2} \int_0^L B_{\parallel}(l) n_e(l) dl \quad (22)$$

where the rotation measure RM is defined to be the integration of the electron number density  $n_e(l)$  with the ISM magnetic field component that is parallel to the direction of propagation  $B_{\parallel}(l)$  at each distance increment  $dl$  along the path of the medium with thickness of  $L$ . The other physical constants are the charge of an electron  $e$ , electron mass  $m_e$ , and the speed of light in vacuum  $c$ .

Due to irregular distribution of electron density in the ISM as well as the Galactic magnetic field, the frequency-dependent Faraday rotation of the incoming polarized foreground emission will be different across the band. Hence, unwanted spectral structures can also be intro-

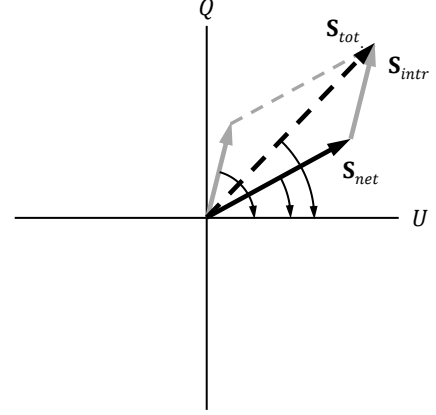


FIG. 21.— Intrinsic foreground polarization  $\mathbf{S}_{intr}$  (solid gray) contributes to the projection-induced polarization  $\mathbf{S}_{net}$  (solid black) as a vector summation. Since the intrinsic polarization follows the foreground rotation, the resulting total measured polarization  $\mathbf{S}_{tot}$  (dashed black) also contains a second harmonic component which can be used to constrain the foreground spectrum.

duced to the measured spectrum. In fact, the intrinsic foreground polarization has been identified as the main cause of the polarization leakage which complicates the instrument calibration in the interferometric EoR experiments (Jelić et al. 2014, 2015; Asad et al. 2015).

A single polarization dipole system in conventional global experiment may be insensitive to linearly polarized portion of the foreground emission if the antenna is not aligned with the orientation of the foreground polarization. On the other hand, a full-Stokes measurement as proposed in this study can measure the intrinsically polarized portion of the foreground and improves the accuracy of the foreground spectrum measurement. Since the intrinsic polarization follows the apparent foreground rotation relative to the antenna on the ground, its contribution to the net projection-induced polarization can be represented as a vector summation between the projection Stokes vector  $\mathbf{S}_{net}$  and the intrinsic Stokes vector  $\mathbf{S}_{intr}$ . As a result, the total measured polarization  $\mathbf{S}_{tot}$  also contains a component of twice the sky revolution rate. A total-power spectrum and a second harmonic spectrum can be reconstructed as before. Assuming only the polarizations are linear, Figure 21 illustrates the vector summation between Stokes vectors can be represented by a 2-D version of the Poincaré sphere with the  $Q$  and  $U$  axes.

### 5.9. Foreground spectral index variations and detection validation

The foreground continuum emission has been observed to have a direction-dependent spectral index  $\beta$  depending on the pointing, i.e.,  $\beta = \beta(\theta, \phi)$ . The spectral index distribution can be estimated by extrapolating from a power law between the Haslam all-sky survey at 408 MHz and a 45 MHz map (Guzmán et al. 2011) as shown in Figure 22. This may potentially complicate the foreground measurement using the second-harmonic Stokes spectrum. By writing Equation (23) with a non-constant  $\beta$  as

$$T_{fg}(\theta, \phi, \nu) = T_{\text{Haslam}}(\theta, \phi) \left( \frac{\nu}{408 \text{ MHz}} \right)^{-\beta(\theta, \phi)} \quad (23)$$

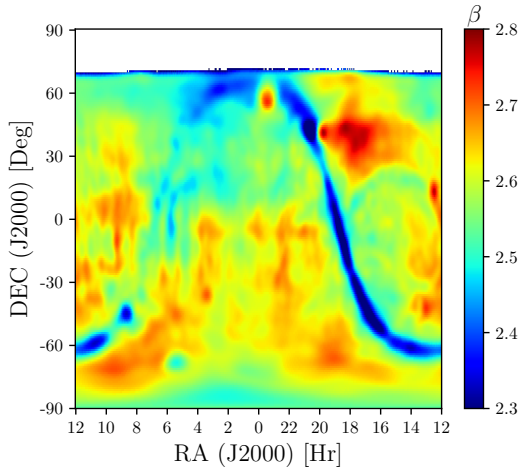


FIG. 22.— Foreground spectral index distribution is obtained from extrapolating between the Haslam all-sky survey at 408 MHz and a 45 MHz map. The missing data around the NCP represents  $\sim 4\%$  of the whole sky in the 45-MHz map.

it is apparent the chromatic antenna beam pattern can couple to the sky differently at different frequencies. As a result, the net projection-induced polarization can vary and contribute some unwanted spectral feature to the Stokes spectra, especially the second-harmonic one, if the antenna beam is not corrected.

However, since the induced-polarization approach measures both the total-power spectrum and the second harmonic spectrum simultaneously from the same sky region, as the simulations suggested, the measured mean spectral index of  $S_{Q,2}^\nu$  is still identical to the foreground spectral index in  $S_{I,0}^\nu$  for any given mean value of  $\beta$  averaged over the sky. In fact, one of the biggest challenges for the global signal experiment is to ensure such any spectral structures detected in the residual are indeed from the background signal. This degeneracy can be broken by carrying out multiple observation at different sky regions. For example, on the ground, if the residual spectral features measured at the NCP and SCP are consistent, they are very likely originated from the same source, and possibly the background itself.

#### 5.10. RFI and ionospheric distortion

One of the major sources of contamination is RFI. Traditionally, radio-quiet sites, such as South Africa’s Karoo desert and Murchison Radio-Astronomy Observatory in Western Australia, are chosen for minimal contamination. Recently, DARE proposed to carry out observations on the lunar farside when the spacecraft orbits around the Moon (Burns et al. 2012). Nonetheless, regardless how quiet a site is, there is always low-level RFI which is either reflected or scattered from satellites, space debris, and the ionosphere (Offringa et al. 2013).

A common practice is to utilize RFI excision algorithm, such as one based on kurtosis of the incoming signal’s statistics (Antoni 2004; De Roo 2009; Nita & Gary 2010), to remove the corrupted signal channels. This approach is more effective to detect the strong instead of the low-level RFI, especially ones that are equivalent to the system’s noise level. Hence, unknown spectral structures can also be introduced to the measured spectrum. However, since most of the incoming RFI are

direction-dependent, they do not necessarily introduce any dynamic variations to the measured linear Stokes parameters, unless they are affected by the ionosphere during propagation. More importantly, the RFI does not contain a  $n = 2$  component, hence does not have a major effect on the second-harmonic spectrum used to constrain the foreground spectrum.

The ionosphere has been well known for causing refraction, absorption, and self-emission to radio propagation. Not until recently that careful studies have started investigating the effects of ionospheric distortion to the ground-based 21-cm measurements (Vedantham et al. 2013; Datta et al. 2016; Sokolowski et al. 2015b; Rogers et al. 2015). The ionosphere consists of plasma layers with complex structures whose characteristics are position and time dependent. The total electron content (TEC), which represents the total electron column density for a given direction, varies throughout the day. These variations are pseudo-periodic from one day to another, but not repeatable and difficult to quantify. Current total-power global 21-cm experiments (Sokolowski et al. 2015b; Rogers et al. 2015) have only provided limited understanding on how these ionospheric effects can impact the accuracy and precision of the global 21-cm signal. Attempts to utilize Global Positioning System (GPS) ionospheric measurements are considered insufficient to calibrate the ionospheric effect (Datta et al. 2016). However, by measuring the dynamic ionospheric variations, our polarimetric approach may provide some constraints on their influence on the overall sky measurement as a function of time and observed frequency. A more thorough study in this area will be conducted in future work.

#### 5.11. Summary

We have shown that the harmonic decomposition of the dynamic Stokes parameters provides additional information on different types of measurement and systematic uncertainties. In most cases, the experiment can be designed and configured to modulate the foreground measurement in attempt to distinguish these perturbations from the signal of interest. Based on our simulations and analysis, Table 2 provides a rudimentary list of harmonic components that can potentially be used to identify different signal sources and bound the uncertainty in constraining the foreground spectrum. Harmonics at higher orders ( $n > 4$ ) are indicated as “H” for reference.

In analogy to the CMB anisotropy studies (i.e., Tegmark & Efstathiou 1996; Ichiki 2014), the foreground spatial anisotropy and hence its induced-polarization can also be decomposed into spherical harmonic  $Y_l^m(\theta, \phi, \nu)$  with different modes  $l = 0, 1, 2, \dots$  and  $m = 0, \dots, l$ . We speculate that such decomposition is complimentary to the harmonic analysis. In fact, by combining the two, it may be possible to characterize different contribution and systematics in the measurement by mapping out different modes and harmonics, similar to Table 2. This is outside the scope of the current study.

#### 6. CONCLUSION

A new observational approach is proposed to constrain the foreground spectrum through measuring the projection-induced polarization of the foreground anisotropy without assuming any sky model. Harmonic

TABLE 2  
SUMMARY OF HARMONIC ANALYSIS FOR THE PROJECTION-INDUCED STOKES SPECTRA.

Signal Sources Stokes Spectrum:	Harmonic Order $n$					Notes
	$S_I^\nu$	$S_{I_p}^\nu$	$S_Q^\nu$	$S_U^\nu$	$S_V^\nu$	
21-cm background	0	...	...	...	...	for circular Gaussian beams
Projection-induced polarization	...	...	2	2	...	for circular Gaussian beams
Beam gain distortion & elongation	0, 4	4	H <sup>a</sup>	H	H	need correction with beam models
Horizon obstruction	0, 1	1	1	1	1	latitude & sky dependent
Boresight pointing error	4	4	H	H	H	
RFI	0	H	H	H	H	location & time dependent
Ionospheric distortion	0	H	H	H	H	time & latitude dependent, pseudo-periodic

<sup>a</sup>H - possible high-order harmonics, i.e.,  $n > 4$

analysis of the induced Stokes vector measured as a function of time plays a key role in separating the dynamic foreground component from the static background. The harmonic analysis also provides additional information on instrumental systematics, and external contaminants such as RFI and ionospheric distortions. This study established a framework for developing our team's upcoming ground-based prototype, the Cosmic Twilight Polarimeter (CTP), which will allow us to explore some of the implementation aspects listed above to further evaluate our approach.

By assuming an idealized instrument with a Gaussian beam, free from RFI and ionospheric distortion, and the absorption feature of the 21-cm spectrum is present in the instrument passband, some of the key aspects we found are:

- The spectral dependence of the foreground spectrum can be robustly measured in terms of the second-harmonic Stokes spectra  $S_{Q,2}^\nu$  and  $S_{U,2}^\nu$  retrieved from the frequency-dependent cyclic signature in the projection-induced polarization when the FOV is centered at a celestial pole.
- The blind search for zero-crossing from the first derivative of the background 21-cm spectrum provides a unique initial condition in solving for the scaling factor between the Stokes spectra to be used for foreground subtraction, even without any knowledge of the background signal.
- Chromatic distortion from the frequency-dependent antenna beam is one of the main instrumental effects that introduced unwanted spectral structures to confuse the foreground and the global 21-cm spectra. Careful beam calibration procedures, such as using beam models generated by sophisticated electromagnetic propagation

simulation software and direct beam measurement, are required.

- Environment factors and observation configuration, like ground effects and pointing error, contribute variations and confusions to the measurements in this polarimetric approach. Realistic assessment on instrument design and setup will help increasing the measurement sensitivity for the Stokes spectra.
- As long as the foreground spectra from different sky regions, such as ones about the NCP and SCP, can be measured and subtracted independently, recovered global spectral structures will be consistent to a common homogeneous 21-cm background. This helps eliminating observational ambiguity and increases detection likelihood of the global 21-cm signal.

## 7. ACKNOWLEDGMENTS

The National Radio Astronomy Observatory is a facility of the National Science Foundation operated under cooperative agreement by Associated Universities, Inc. Support for this work was provided by the NSF through the Grote Reber Fellowship Program administered by Associated Universities, Inc./National Radio Astronomy Observatory. This research was also supported by the NASA Ames Research Center via Cooperative Agreements NNA09DB30A, NNX15AD20A, and NNX16AF59G to J. O. Burns. The authors like to especially thank J. Aguirre for his constructive feedback on the formalism of our approach and discussions on other aspects related to the foreground polarization. The authors would also like to thank R. Monsalve for his comments on the instrumental aspects of the approach. The authors gratefully acknowledge J. Mirocha for providing the simulated global 21-cm data using ARES. B. D. Nhan is also grateful to K. Tauscher and R. Monsalve for their assistance in utilizing the sky map data.

## REFERENCES

- Antoni, J. 2004, 1167  
 Asad, K. M. B., Koopmans, L. V. E., Jelić, V., et al. 2015, MNRAS, 451, 3709  
 Balanis, C. A. 2016, Antenna Theory: Analysis and Design (John Wiley & Sons)  
 Bernardi, G., McQuinn, M., & Greenhill, L. 2015, The Astrophysical Journal, 799, 90  
 Bittner, J. M., & Loeb, A. 2011, Journal of Cosmology and Astroparticle Physics, 4, 38  
 Bowman, J. D., & Rogers, A. E. 2010, Nature, 468, 796  
 Bowman, J. D., Rogers, A. E., & Hewitt, J. N. 2008, The Astrophysical Journal, 676, 1  
 Bowman, J. D., Cairns, I., Kaplan, D. L., et al. 2013, Publications of the Astronomical Society of Australia, 30, e031  
 Burns, J. O., Lazio, J., Bale, S., et al. 2012, Advances in Space Research, 49, 433  
 Datta, A., Bradley, R., Burns, J. O., et al. 2016, ApJ, 831, 6  
 De Roo, R. D. 2009, IEEE Transactions on Geoscience and Remote Sensing, 47, 3755

- Furlanetto, S. R. 2006, *Monthly Notices of the Royal Astronomical Society*, 371, 867
- Furlanetto, S. R., Oh, S. P., & Briggs, F. H. 2006, *Physics Reports*, 433, 181
- Greenhill, L. J., & LEDA Collaboration. 2015, in *American Astronomical Society Meeting Abstracts*, Vol. 225, *American Astronomical Society Meeting Abstracts*, 403.07
- Guzmán, A. E., May, J., Alvarez, H., & Maeda, K. 2011, *Astronomy & Astrophysics*, 525, A138
- Hamming, R. 2012, *Numerical Methods for Scientists and Engineers* (Courier Corporation)
- Harker, G. J. 2015, *Monthly Notices of the Royal Astronomical Society: Letters*, 449, L21
- Harker, G. J., Pritchard, J. R., Burns, J. O., & Bowman, J. D. 2012, *Monthly Notices of the Royal Astronomical Society*, 419, 1070
- Haslam, C., Salter, C., Stoffel, H., & Wilson, W. 1982, *Astronomy and Astrophysics Supplement Series*, 47, 1
- Heiles, C. 2002, 278, 131
- Heinzel, G., Rüdiger, A., & Schilling, R. 2002
- Ichiki, K. 2014, *Progress of Theoretical and Experimental Physics*, 2014, 06B109
- Jelić, V., De Bruyn, A., Mevius, M., et al. 2014, *Astronomy & Astrophysics*, 568, A101
- Jelić, V., de Bruyn, A., Pandey, V., et al. 2015, *Astronomy & Astrophysics*, 583, A137
- Johnson, B., Collins, J., Abroe, M., et al. 2007, *The Astrophysical Journal*, 665, 42
- Kogut, A. 2012, *The Astrophysical Journal*, 753, 110
- Kraus, J. D. 1986, *Radio Astronomy*
- Kusaka, A., Essinger-Hileman, T., Appel, J., et al. 2014, *Review of Scientific Instruments*, 85, 024501
- Liu, A., Pritchard, J. R., Tegmark, M., & Loeb, A. 2013, *Physical Review D*, 87, 043002
- Mahesh, N., Subrahmanyan, R., Shankar, N. U., & Raghunathan, A. 2014, arXiv preprint arXiv:1406.2585
- Mellema, G., Koopmans, L. V., Abdalla, F. A., et al. 2013, *Experimental Astronomy*, 36, 235
- Mirocha, J. 2014, *Monthly Notices of the Royal Astronomical Society*, 443, 1211
- Mirocha, J., Furlanetto, S. R., & Sun, G. 2017, *MNRAS*, 464, 1365
- Mirocha, J., Harker, G. J., & Burns, J. O. 2013, *The Astrophysical Journal*, 777, 118
- . 2015, *The Astrophysical Journal*, 813, 11
- Mozdzen, T. J., Bowman, J. D., Monsalve, R. A., & Rogers, A. E. 2016, *Monthly Notices of the Royal Astronomical Society*, 455, 3890
- Newell, P. T., Greenwald, R. A., & Ruohoniemi, J. M. 2001, *Reviews of Geophysics*, 39, 137
- Nita, G. M., & Gary, D. E. 2010, *Monthly Notices of the Royal Astronomical Society: Letters*, 406, L60
- Offringa, A., De Bruyn, A., Zaroubi, S., et al. 2013, *Monthly Notices of the Royal Astronomical Society*, stt1337
- Paciga, G., Albert, J. G., Bandura, K., et al. 2013, *Monthly Notices of the Royal Astronomical Society*, stt753
- Parsons, A. R., Pober, J. C., Aguirre, J. E., et al. 2012, *The Astrophysical Journal*, 756, 165
- Parsons, A. R., Backer, D. C., Foster, G. S., et al. 2010, *The Astronomical Journal*, 139, 1468
- Patra, N., Subrahmanyan, R., Raghunathan, A., & Shankar, N. U. 2013, *Experimental Astronomy*, 36, 319
- Petrovic, N., & Oh, S. P. 2011, *Monthly Notices of the Royal Astronomical Society*, 413, 2103
- Pober, J. C., Liu, A., Dillon, J. S., et al. 2014, *ApJ*, 782, 66
- Pritchard, J. R., & Loeb, A. 2010, *Phys. Rev. D*, 82, 023006
- Pritchard, J. R., & Loeb, A. 2012, *Reports on Progress in Physics*, 75, 086901
- Rogers, A. E., Bowman, J. D., Vierinen, J., Monsalve, R., & Mozdzen, T. 2015, *Radio Science*, 50, 130
- Shaver, P. A., Windhorst, R. A., Madau, P., & de Bruyn, A. G. 1999, *A&A*, 345, 380
- Sokolowski, M., Tremblay, S. E., Wayth, R. B., et al. 2015a, *Publications of the Astronomical Society of Australia*, 32, e004
- Sokolowski, M., Wayth, R. B., Tremblay, S. E., et al. 2015b, *The Astrophysical Journal*, 813, 18
- Switzer, E. R., & Liu, A. 2014, *ApJ*, 793, 102
- Tegmark, M., & Efstathiou, G. 1996, *MNRAS*, 281, 1297
- Tegmark, M., Eisenstein, D. J., Hu, W., & de Oliveira-Costa, A. 2000, *The Astrophysical Journal*, 530, 133
- Tingay, S., Goeke, R., Bowman, J. D., et al. 2013, *Publications of the Astronomical Society of Australia*, 30, e007
- Tripe, S. 2014, *Journal of the Korean Astronomical Society*, 47, 15
- Van Haarlem, M., Wise, M., Gunst, A., et al. 2013, *Astronomy & astrophysics*, 556, A2
- Vedantham, H., Koopmans, L., de Bruyn, A., et al. 2013, *Monthly Notices of the Royal Astronomical Society*, stt1878
- Voytek, T. C., Natarajan, A., García, J. M. J., Peterson, J. B., & López-Cruz, O. 2014, *The Astrophysical Journal Letters*, 782, L9
- Wilson, T. L., Rohlfs, K., & Hüttemeister, S. 2009, *Tools of Radio Astronomy*, Vol. 86 (Springer)
- Wolleben, M., Landecker, T., Reich, W., & Wielebinski, R. 2006, *Astronomy & Astrophysics*, 448, 411